

The dynamic association of SPO11-1 with conformational changes of meiotic axial elements in maize

Short title: Axial element structure and dynamic SPO11-1 localization

Arnaud Ronceret^{1,2¶}, Inna Golubovskaya^{1,3¶}, Jia-Chi Ku^{4¶}, Ding Hua Lee⁴, Ljudmilla Timofejeva^{1,#a}, Ana Karen Gomez Angoa², Yu-Hsin Kao⁴, Karl Kremling^{1,#b}, Rosalind Williams-Carrier⁵, Robert Meeley⁶, Alice Barkan⁵, W Zacheus Cande¹, and Chung-Ju Rachel Wang^{4*}

¹ Department of Molecular and Cell Biology and Plant and Microbial Biology, 341 LSA, University of California, Berkeley, CA 94720-3200, USA.

² Instituto de Biotecnología / UNAM Cuernavaca, Morelos 62210, Mexico.

³ N.I. Vavilov Institute of Plant Industry, St.-Petersburg 190000, Russia.

⁴ Institute of Plant and Microbial Biology, Academia Sinica, Taipei 11529, Taiwan.

⁵ Institute of Molecular Biology, University of Oregon, Eugene, OR 97403, USA.

⁶ Corteva Agriscience, Agriculture Division of DowDuPont, Johnston, Iowa 50131-1004, USA.

¶ These authors contributed equally to this work.

#a Current address: Institute of Experimental Botany ASCR, Prague 16502, Czech.

#b Current address: Inari Agriculture, Cambridge, MA 02139, USA

*Corresponding authors: rwang@gate.sinica.edu.tw

Abstract

Double strand breaks (DSBs) are generated at the beginning of meiosis by the evolutionarily conserved SPO11 complex that targets preferentially open chromatin. However, how DSBs are formed with respect to chromosome axes in a timely controlled manner remain unclear. Here, we analyzed the maize *spo11-1* mutant and show that it strongly impairs DSB and bivalent formations. Notably, cytological characterization in the *spo11-1* mutant revealed abnormally twisted axial elements that persisted until pachytene. In contrast, examinations of precisely staged wild-type meiocytes uncovered a transient remodeling of axial elements, changing from a curly to linear morphology during leptotene to zygotene transition, which is coincident with DSB formation. Using a SPO11-1 antibody, approximately 300 foci were detected from leptotene to pachytene in wild-type meiocytes. Interestingly, when examining distances between SPO11-1 foci to chromosome axes by super-resolution microscopy, predominant loading of SPO11-1 onto axial elements occurs concordantly with alteration of axial elements during leptotene. Taken together, our results suggest a dynamic localization of SPO11-1 during early meiosis that is correlated with a remodeling of the axial element conformation.

Author Summary

Meiosis is an important step in sexual reproduction for producing haploid gametes. Recombination is the most crucial step during meiotic prophase I, which enables pairing of homologous chromosomes prior to their reductional division, and generates new combinations of genetic alleles for transmission to the next generation. Meiotic recombination is initiated by generation of many DNA double-stranded breaks (DSBs), and their repair leads to reciprocal exchanges between paternal and maternal chromosomes. The activity, timing and location of this

DSB machinery must be controlled precisely, but a full picture is still obscure. By studying maize SPO11-1, a topoisomerase-related enzyme required for making DSBs, we uncovered dynamic localization of SPO11-1 that is correlated to a transient structural change of the axial elements of wild-type plant meiocytes by super-resolution microscopy. Interestingly, loss of SPO11-1 impairs this structural change, resulting in a prolonged spiral morphology. Our study suggests an intimate relationship between SPO11-1 and axial elements and has implications for our understanding of how DSB formation is controlled in plants.

Introduction

Meiosis is a special type of cell division that includes two successive nuclear divisions after one round of DNA replication and it allows segregation of only one copy of homologous chromosomes to halve the ploidy number. A faithful segregation of chromosomes requires meiotic recombination during prophase I, which mediates pairing of homologous chromosomes and creates physical connections until their segregation (1). Meiotic recombination is initiated by the introduction of double strand breaks (DSBs) into chromosomal DNA by SPO11, a protein belonging to a distant topoisomerase VI family (2). Absence of SPO11 results in defective initiation of meiotic recombination in all species analyzed, leading to sterile phenotype.

The self-inflicted DNA breaks introduced by SPO11 are tightly controlled both temporally and spatially to allow proper initiation of recombination (1). These DSBs must be repaired to ensure genome integrity. Only a small subset of DSBs produces crossovers (COs) that involve long reciprocal exchanges between homologous chromosomes, whereas the residual DSBs lead to non-crossovers (NCOs) (3). These CO sites, seen as chiasmata at diplotene stage, ensure that the pairs of homologs, i.e. the bivalents, maintain their association and align properly at the metaphase plate, which allows the following reductional segregation at the anaphase I.

Thus, at least one CO per bivalent is needed for an equilibrated reductional division. Too few DSBs could be detrimental since sufficient DSBs are required for homolog engagement in most species. However, too many DSBs can also be deleterious since they may result in chromosome fragmentation if unrepaired. Therefore, DSB formation is restricted to a narrow window of time with regulatory mechanisms controlling DSB numbers.

Remarkably, DSBs are not uniformly distributed along chromosomes, and regions called 'hot spots' and 'cold spots' show higher or lower DSB frequencies, respectively (4). Maps of recombination initiation have been analyzed at a genome-wide level in *S. cerevisiae*, mice, human, *Arabidopsis* and maize (5-10). Despite the diversity found among species, a common feature of DSB hotspots seems to be epigenetically marked open chromatin (11). For example, DSB hotspots in budding yeast are predominantly in nucleosome-depleted regions in gene promoters (10). In mammals, DSB hotspots are enriched with histone H3K4me3 modification that is deposited by the PRDM9 methyltransferase (12). Recent studies in maize and *Arabidopsis* have also revealed that DSB hotspots are correlated with low nucleosome occupancy and low DNA methylation. Interestingly, DSBs are not only located in genic regions but also in DNA transposons of *Arabidopsis* and retrotransposons of maize, which is different from a general concept that repetitive sequences are 'cold' for DSB formation (8, 9).

Although how the DSB machinery functions is not yet clear, several axis-located proteins such as Rec114, Mer2, Red1, Hop1 and Mei4 in yeast were found to be required for DSB formation (13). These findings suggest that the DSB machinery associated with chromosome axes somehow activates SPO11 transesterase activity. However, DNA sequences prone to DSBs have been mapped to loop domains away from the axis-associated sequences (14). Thus, a 'tethered loop-axis complex' model has been postulated in an attempt to reconcile these findings, which argues for a transient, but as yet unobserved, localization of the SPO11 complex toward

the axial elements (AEs) during DSB formation (5, 15). In *S. pombe*, the Rec12/Spo11 recombination complex has been identified, but some of the components are not direct orthologs of the *S. cerevisiae* proteins (16). Interestingly, the *S. pombe* protein Mde2, which is considered an ortholog of Red1 protein, physically links the Spo11 complex with the axial protein Rec10. This finding suggested that a mechanism tethering DSBs in chromatin loops to AEs may be conserved among different species (17).

The meiotic AEs contain specific meiotic cohesin protein REC8 (an ortholog of AtSYN1 and ZmAFD1) that is well conserved among species (18-20). Other meiotic AE proteins have been found to rapidly evolve among species. In plants, ASY1/PAIR2 is likely the functional homolog of HOP1 (21, 22). In mammals, Hop1 is represented by two orthologs HORMAD1 and HORMAD2 (23). These axial proteins contain a HORMA domain and preferentially associate with unsynapsed chromosome axes (22, 24, 25). In addition, mammalian SYCP2 and SYCP3 are integral components of AEs and exhibit limited homology to Red1 (26, 27). The plant PAIR3/ASY3/DSY2 proteins containing coiled-coil domains are likely the functional homolog of Red1 (28-30). Importantly, many of these plant axial proteins are essential for normal DSB formation, such as PAIR3/ASY3/DSY2, PCH2/CRC1 (31, 32) and P31^{comet} (33).

How DSB formation is controlled remains poorly understood with respect to the activation and attenuation of the SPO11 complex, as well as its relationship to AE proteins. The 'tethered loop-axis complex' model explains that DSB sites are tethered with chromosomes axes (34); however, cytological evidence has been scarce. In addition, upon DSB induction in the context of loop-axis structure, how the axis is responsive, if any, to DSB formation? In species such as maize, barley, and wheat with large chromosomes, subtle and transient changes of chromosome structure and AE morphology can be more easily observed than in species with small chromosomes (35-40). Here, we show that maize *Spo11-1* is, as expected, required for DSB

and bivalent formation. Interestingly, cytological analysis of the *spo11-1* mutant exhibited an unexpected phenotype, with AEs exhibiting a spiral morphology from leptotene through late zygotene. In contrast, in wild-type meiocytes, a transient AE conformational change was observed during late leptotene, which coincides with an increase of SPO11-1 number associated with AEs. These findings provide the first cytological evidence of dynamic SPO11-1 localization during DSB formation and suggest that a possible SPO11-1 dependent mechanism may orchestrate changes in AE structures.

Results

The two maize meiotic mutants *mtm99-14* and *mtm00-03* are allelic

We used a forward genetic approach to identify genes involved in the control of the maize meiotic program based on sterility and meiotic cytological analysis (25, 41, 42). Among the meiotic mutants, the *mtm99-14* and *mtm00-03* mutants exhibited severe male and female infertility (Fig 1A and 1B). Wild-type (WT) sibling plants self-pollinated can produce full seed sets, whereas neither homozygous mutant produced seeds after self-pollination. When *mtm99-14* and *mtm00-03* mutants were manually pollinated with WT pollens, both mutants produced one or two kernels (0.17 % of 1152 ovules for *mtm99-14* and 0.07% of 1421 ovules for *mtm00-03*). We found that *mtm99-14* and *mtm00-03* are allelic based on segregation for the male and female sterile phenotype among the F1 progeny in an allelism test. The heteroallelic *mtm99-14/mtm00-03* plants are male sterile and manual pollination of their female ears with WT pollens produced no or few kernels (0.12% of 1624 ovules).

We then analyzed meiotic progression of homozygous *mtm99-14*, *mtm00-03* and heteroallelic *mtm99-14/mtm00-03* mutants in detail. In the WT, ten bivalents align on the metaphase plate during metaphase I, but mutants contain mainly univalents with 5-7% of

meiocytes forming one or few bivalents (Fig 1C, upper panel, and 1D). In contrast to normal tetrad cells in WT, abnormal microspores are seen as unequal tetrads, as tetrads with micronuclei, or as polyads in mutants (Fig 1C, lower panel, and 1E). This phenotype indicates that both *mtm99-14* and *mtm00-03* exhibit impaired bivalent formation and the resulting univalents randomly segregate, leading to the formation of unequal spores and inviable pollens.

The strong sterility of maize ears indicates that female meiosis is affected similarly to that of males. That few seeds were obtained from homozygous mutants when pollinated with WT pollens indicates that these mutants can only produce rare viable female megaspores. In maize asynaptic mutants, the probability of obtaining viable spores with the full haploid set of ten chromosomes from random segregation is 0.12% ($1/2^{10}$). The proportion of seeds obtained from these mutants pollinated by WT pollens is not statistically different from the expected proportion of completely random segregation ($\epsilon = 0.82$ for *mtm99-14*, $\epsilon = 0.32$ for *mtm00-03*, $\epsilon = 0.33$ for *mtm99-14/mtm00-03* $< \epsilon_{\alpha 5\%} = 1.96$). This analysis demonstrates that the male and female infertility of *mtm99-14* and *mtm00-03* is due to severe defects of bivalent formation.

***mtm99-14* and *mtm00-03* mutants exhibit deletions of the *Spo11-1* locus associated with Mu insertions**

The *mtm00-03* mutant was first mapped to chromosome 5 by molecular markers (see Material and Methods). To identify the gene, we used the Mu-Illumina strategy to analyze Mu insertion borders that cosegregate with sterile phenotype (43) and found that *mtm99-14* mutant contains Mu element sequences inserted into a Tourist transposable element that is located 9 kb upstream of the *Spo11-1* gene (*GRMZM2G129913/ZM05G04150*) on maize chromosome 5. Similarly, *mtm00-03* mutant carries a Mu insertion about 4 kb upstream of the *Spo11-1* gene (Fig 2A). These Mu sequences in both mutants are associated with deletions, which likely resulted

from Mu-induced excisions. Both deletions span the *Spo11-1* and *phytochrome C2* genes (*PhyC2*: GRMZM2G129889/ZM05G04160). We could not determine the lengths of deletions and only one Mu border was recovered in our Mu-Illumina sequence analyses. Nevertheless, reverse transcription (RT) PCR experiments confirmed that neither of the *mtm99-14* or *mtm00-03* mutants expressed the *Spo11-1* gene in meiotic anthers (Fig 2B). Upon examining *PhyC2* expression by RT-PCR, we detected an unexpected signal in both mutants (Fig S1). Further sequence analysis showed that the resulting DNA fragment in the *mtm99-14* and *mtm00-03* mutants was amplified from the paralogous *PhyC1* (GRMZM2G057935/ZM01G52970), which is located on chromosome 1 and shares 94% identity with the *PhyC2* coding region. Given this high similarity, our primers were unable to distinguish the *PhyC1* and *PhyC2* coding sequences.

Considering the complex rearrangements that may occur in both *mtm99-14* and *mtm00-03*, we searched for other mutations affecting only the *Spo11-1* gene. From the Trait Utility System for Corn (TUSC) transposon mutagenesis population (44), one additional mutant, named *spo11-1-1* contains a Mu insertion located in the first exon (Fig 2A) and exhibits male and female infertility. Cytological analyses of male meiosis in this mutant also exhibited 20 univalents in most meiocytes, and similarly to *mtm99-14* and *mtm00-03*, 5% of meiocytes exhibited one or two bivalents (Fig 1D and S2). Allelism tests between *mtm99-14/+* or *mtm00-03/+* and *spo11-1-1/+* further confirmed that they are allelic. Thus, *mtm99-14* and *mtm00-03* are renamed to *spo11-1-Δ14* and *spo11-1-Δ03*, respectively. Since all alleles exhibited an identical phenotype, the results of *spo11-1-Δ03* are shown in main figures and results for other alleles are included in Figures S2, S6, and S7.

Maize *Spo11-1* gene exhibited alternative splicing

Our analysis of *Spo11-1* gene expression by RT-PCR detected different spliced variants

(Fig 2B) and found that the variability arose from retention of the second intron (Fig 2D). Both transcripts are predicted to produce functional SPO11-1 proteins because they contain a nuclear localization signal (KLRR) in the N terminal region, the topoisomerase-primase ‘TOPRIM’ domain that is essential for catalytic activity, and the conserved tyrosine residue in the winged-helix DNA-binding (WHD) domain (Fig 2E). The longer transcript (named *Spo11-1 β*) encodes a 426 amino acid protein that contains an extra 43 amino-acid domain translated from the intron 2 (Fig 2D, 2E, S3). This additional region is predicted to form an alpha-helix motif upstream of the TopVIA type endonuclease domain (Fig S4).

We designed transcript-specific primers (shown in Fig 2D) to examine temporal expression patterns of different transcripts. Quantitative PCR results revealed that the *Spo11-1 β* transcript is about twice as abundant as the *Spo11-1 α* transcript in leptotene/zygotene anthers, whereas *Spo11-1 α* is expressed slightly more before prophase I (Fig 2C). In order to understand whether both splicing variants can produce SPO11-1 protein isoforms, we generated a SPO11-1 antibody using an N-terminal peptide (aa 9-36). Using proteins extracted from meiotic anthers of WT and *spo11-1- Δ 03* plants, we detected two weak bands (arrowheads in Fig 2F) between 35-40 kDa in WT, which are absent in the mutant samples (Fig 2F). The entire blot is shown in the Fig S5). This result suggested that two SPO11-1 isoforms are produced in meiotic anthers. Unfortunately, our attempts to further examine these two isoforms by generating isoform-specific antibodies were not successful.

The *spo11-1* maize mutants are defective in DSB formation

Since SPO11-1 is required to initiate homologous recombination by creating DSBs, we determined cytologically whether the *spo11-1* mutants are defective for meiotic DSBs. The terminal deoxynucleotidyl transferase dUTP nick end labeling (TUNEL) assay was used to detect

DNA free ends associated with DSBs. Compared to obvious signals detected in WT meiocytes at zygotene, we found that most of *spo11-1* meiocytes did not show any TUNEL signals on chromatin (Fig 3A). Only around 10% of the mutant meiocytes had a few TUNEL foci usually located in one region of the nucleus (n=7/74: 9.5% for *spo11-1-Δ14*, n=2/24: 8.3% for *spo11-1-Δ03* and n=5/42: 11.9% for *spo11-1-1*) (Fig S6). These few DSBs may explain the rare observation of bivalents in maize *spo11-1* mutants (Fig 1D and S2), suggesting that a minor SPO11-1 independent pathway can lead to rare bivalent formations in maize.

To further confirm DSB formation defects, we applied antibodies against γ H2AX, Replication Protein A1 (RPA1a), and RAD51 proteins. In various eukaryotes, phosphorylation of the histone variant H2AX (γ H2AX) is induced rapidly at DSB sites. Then, RPA1 interacts with the single-stranded DNAs after DSB resection and, later, loading of the recombinase RAD51 facilitates recombination. In WT male meiocytes, γ H2AX signals appeared at early zygotene, observed as numerous dots on maize chromosomes. In contrast, most of *spo11-1* meiocytes exhibited no γ H2AX signals (Fig 3B). Numbers of RPA1a and RAD51 foci in WT peaked during mid-zygotene, whereas most of the mutant meiocytes completely lacked signals (Fig 3C and 3D). Similarly, around 10% of the mutant cells showed few RAD51 foci on chromatin (n=3/34: 8.8% for *spo11-1-Δ14*, n=4/37: 10.8% for *spo11-1-Δ03* and n=2/22: 9.1% for *spo11-1-1*), which is consistent with our TUNEL results (Fig S6). Thus, we concluded that maize SPO11-1 is required for normal DSB formation.

Maize *spo11-1* mutants present an aberrant, twisted axial element structure

In maize, meiosis in anthers of similar sizes is almost synchronous during prophase I, and the relative positions of anthers on a maize tassel are correlated to their developmental stages. Thus, anther sizes and their positions on a tassel provide a relative time course for meiotic

progression, i.e. meiosis in 2 mm anthers is more progressed than it is in 1.5 mm anthers on the same tassel. To follow recombination along meiotic progression, we dissected anthers from the same tassel in order and used anthers of the same size to prepare slides for immunostaining. Therefore, our analyses provide adequate temporal resolution, which allows a detailed characterization of the course of recombination initiation.

Previous studies have shown that maize meiotic chromosome axes labeled with DSY2 and ASY1 antibodies appear as linear central cores along chromosomes at zygotene (29). Surprisingly, *spo11-1* meiocytes exhibited twisted DSY2 and ASY1 signals (Figs 4B, 4C, S7). To investigate this phenotype in detail, we examined axes morphology at very early stage when axial elements first appear and enclose a nucleolus in the center. We noticed that at early leptotene, AEs exhibited a similar curly appearance in both WT and *spo11-1* mutants (Fig 4A). The twisted axes are more evident when visualized through z-sections (Movies S1, S2). At late leptotene/early zygotene, when nucleolus is offset inside the nucleus, AEs in WT meiocytes become smoother and linear in most parts of chromosomes. However, unlike WT AEs that switch to a linear structure at late leptotene, twisted AEs persist in *spo11-1* mutants (Figs 4B, 4C).

Synaptonemal complex is assembled promiscuously in *spo11-1* mutants

In WT maize, upon telomere clustering, synapsis takes place mostly from telomere clustering regions and extends toward to interstitial regions as observed by the transverse filament protein ZYP1 signals (Fig 5A). At pachytene, ZYP1 is loaded along the entire length of synapsed chromosomes (Fig 5C). In contrast, ZYP1 is discontinuously installed first as short stretches in *spo11-1* meiocytes (Fig 5B). Until late pachytene, longer but discontinuous ZYP1 signals were observed in *spo11-1* mutants (Fig 5D).

Using transmission electron microscopy of silver nitrate stained SCs, we observed a similar conformation of abnormal axes in unsynapsed regions in the *spo11-1* mutant (Fig 5F, 5G). In addition, some regions showed obvious promiscuous synapsis. For example, SC is formed within the same axis (arrows in Fig 5f', 5g'). This finding is consistent with short and discontinuous stretches of ZYP1 signals in the immunostaining result (Fig 5D).

Dynamic SPO11-1 localization occurs concordantly with conformational changes of axial elements

To examine SPO11-1 localization, WT meiocytes from early leptotene to pachytene were subjected to immunolocalization. At early leptotene, most of SPO11-1 signals are located around nuclear periphery (Fig 6A, movie S3). Notably, chromatin stained by DAPI at this stage appears curly morphology, which is similar to axial element stained by DSY2 antibody (Fig 4A, movie S1). When chromosome mass is polarized at late leptotene to early zygotene, SPO11-1 signals are distributed in nucleus (Fig 6B, movie S4). At pachytene stage, SPO11-1 signals are still present (Fig 6C, movie S5). However, SPO11-1 antibody only detected a few foci in *spo11-1-Δ03* meiocytes (Fig 6D, movie S6).

The aberrant AE structure in the absence of SPO11-1 suggested an intimate relationship between SPO11-1 and AEs. To understand the relative dynamics of SPO11-1 and chromosome axes, SPO11-1 and DSY2 localizations were examined by structured illumination microscopy. On average, about 250-350 foci of SPO11-1 were detected during early prophase I in WT (blue boxes in the Fig 6H). In contrast, less than 50 foci were detected in *spo11-1-Δ03* mutant. Although the total number of SPO11-1 foci remained similar during WT leptotene to pachytene, their locations relative to chromosome axes seemed to be dynamic when imaged by super resolution microscopy. When the nucleolus is first offset, some SPO11-1 foci are notably located

around the AE (Fig 6E). At late leptotene with obvious telomere bouquet conformation, more SPO11-1 foci are located on the AE (Fig 6F). Later, in mid-zygotene and pachytene, most of SPO11-1 foci are away from the AEs and widely distributed in the nucleus (Fig S8). Again, the *spo11-1-Δ03* meiocytes exhibited limited SPO11-1 signals (Fig S8).

To investigate their distributions further, we used the software ImageJ to calculate a “distance map” of DSY2 signals in Z stacks and then determined the distances between each SPO11-1 focus to the closest DSY2-labeled axes in 3D space (see material and methods). Among a cohort of meiocytes from an anther during leptotene, we observed leptotene meiocytes with no sign of homologous pairing (e.g. Fig 6E), as well as late leptotene meiocytes with obvious telomere bouquet formation (e.g. Fig 6F). Perhaps, this transition occurs rapidly. Nevertheless, we analyzed leptotene, zygotene and pachytene meiocytes and calculated the numbers of SPO11-1 foci associated with AEs (red boxes in Fig 6H). The leptotene meiocytes showed the highest number of AE-associated SPO11-1 foci, numbers of which gradually decreased in the zygotene and pachytene stages. Furthermore, the highest number of AE-associated SPO11 foci was detected when the AEs become smooth and linear (S2 Table). These results suggest a dynamic localization of SPO11-1 during recombination initiation, which coincides with a conformational change of axial elements.

Discussion

Although maize *spo11-1* mutants exhibited the same meiotic sterility as observed in other species, thanks to the remarkable advantages of maize for cytological observations, our analyses have led to several unexpected results that provide new insights into DSB formation.

The most interesting finding of our study is the twisted AEs observed in the maize *spo11-1* mutant, which prompted us to further examine AE morphology relative to DSB formation.

Using carefully staged WT anthers, our cytological analysis allowed us to visualize a change in AE conformation during the leptotene to early zygotene. Initially at early leptotene, chromatins are organized into curly fibers by axis proteins that appear curly and surround a nucleolus in the center. At this stage, SPO11-1 is mostly located on the nuclear periphery. The twisted AEs observed in maize may reflect the chromosome ‘spiralization’ phenomenon that was described in classical cytological studies during the ‘spiral stage’ of leptotene entry (45). However, this spiral stage is only obvious in species such as lilies or grasshoppers that have huge chromosomes and an extended meiotic prophase (46-48). Even in maize, it has not been reported previously. We interpret the fact that these spiral axes are more easily observed in the mutants than in WT because *spo11-1* mutants have a prolonged leptotene-like stage with curly axes.

It has been reported that the leptotene-zygotene transition (prezygotene) in maize undergoes a dramatic change, including an increase in total chromosome volume, and a peripheral localization and clustering of telomeres (35). Meiotic DSBs are thought to form at this transitional stage (49). Here, we found that when meiocytes exhibited an offset nucleolus, numerous SPO11-1 foci are located inside the nucleus. Then, AEs gradually became smoother and more linear. The remodeling of AE linearization occurs prior to SC assembly in WT, since ASY1 signals that label unsynapsed regions are linear and smooth during WT zygotene (Fig 4C). The presence of curly AEs is not dependent on SPO11-1, since *spo11-1* mutants showed similar curly AEs at the beginning of leptotene. Although the biological role of this transient change in AE morphology (from curly to linear axes) is not yet clear, given the fact that the curly and twisted appearance of AEs persists in maize *spo11-1* mutants, we postulate that the timely remodeling of AEs into linear structures depends on SPO11-1.

As expected, DSB formation is severely affected in maize *spo11-1* mutants, leading to male and female sterility. The fact that SPO11-1 is required for DSB formation raises the

possibility that remodeling of AEs into linear structures may result from DSB occurrence.

However, abnormally twisted AEs have not been reported for other maize mutants that are defective in DSB formation, such as the *dsyCS* mutant (50). Another possibility is that loading of SPO11-1 onto AEs is related to the remodeling of AEs into linear structures. This scenario is somewhat supported by our observations via super-resolution microscopy of dynamic SPO11-1 localization. Interestingly, our analyses showed that leptotene meiocytes have the highest proportion of SPO11-1 foci associated with AEs (Fig 6F). Furthermore, the highest number of AE-associated SPO11-1 signals was found at late leptotene when the AEs become smooth and linear (S2 Table). Nevertheless, mutants in which only DSB formation is disrupted, but SPO11-1 localization is not affected, may be valuable for understanding the nature of AE remodeling.

Another interesting and interlinked finding here was the dynamic nature of SPO11-1 localization. Maize leptotene chromatin is about 400 nm wide and AEs are about 50 nm wide, running along the leptotene chromosomes. Together with our protocol that allows better preservation of the 3D organization of meiotic nuclei, and uses of structured illumination super-resolution microscopy, we were able to resolve SPO11-1 localization in detail. We showed that SPO11-1 appears first on nuclear envelope and then enters nucleus during leptotene. It is first located mostly on chromatin and then loaded on AEs at late leptotene. After zygotene, most SPO11-1 signals are present in nuclei, but not on AEs. To understand whether loading of SPO11-1 on AEs coincides with DSB formation, we sought to examine γ H2AX and SPO11-1 localization. Unfortunately, these antibodies were made in rabbit and proved unsuitable for this purpose. Future investigation using dual immunolocalization will provide a better understanding of SPO11-1 protein localization and DSB formation.

Our observations using super resolution microscopy have revealed for the first time in any organism the dynamic localization of SPO11-1 relative to AEs. We interpret this phenomenon

with regard to the early recombinosome that tethered to axes, i.e. the “tethered loop-axis” model proposed in yeast (5, 15). Perhaps, the curly AEs play an active role in this process. For example, it permits or promotes the tethering process. Later, recombinosomes associated with AEs may be required to activate the DSB machinery. This scenario may explain the defective DSB formation observed in many AE mutants in various species.

Remodeling of AEs into linear axes seems to take place after SPO11-1 loading onto axes or DSB formation in WT. Perhaps, the remodeling of AEs into linear structure prevents more tethering events or additional DSB formation or is related to a reinforcement of inter-homolog recombination bias. Interestingly, yeast Pch2 has been shown to have Hop1 remodeling activity *in vitro* (51). Moreover, yeast Pch2 was suggested to coordinate with the checkpoint protein Tel1^{ATM} to control early DSB formation and to mediate homolog bias (52). In *Arabidopsis*, PCH2 localizes to AEs and is required for normal ASY1 depletion from chromosome axes during SC assembly (31). Although the relationship between DSB formation and AE functions is not yet clear, our study has demonstrated that in the absence of SPO11-1, AE morphology is distinct from that in WT, suggesting an intimate relationship between SPO11-1 and AEs. Our results not only provide the first cytological evidence to support the ‘loop-tethered axis’ model (5), but also shed lights on how DSB formation is controlled in plants.

Material and methods:

Maize material

Maize inbred lines B73, A344, A632 and Mo17, as well as wild type siblings of the Mu insertional mutants and *spo11-1* mutant alleles were grown in the greenhouse of Academia Sinica and previously in the UC Berkeley greenhouse and experimental field. The *mtm99-14 / spo11-1-Δ14* and *mtm00-03 / spo11-1-Δ03* mutants come from two independent genetic screens for maize

meiotic mutants using a Mutator (Mu) population performed, respectively during the 1999 and 2000 field seasons (41, 42). The *spo11-1-1* line was found in the TUSC reverse genetic resource (44).

Genetic mapping and Mu insertion determination.

To map the *mtm00-03* mutation, bulk segregation analysis (BSA) of two *mtm00-03* F2 population created by crossing the *mtm00-03* line with inbred A344 or B73 were used as previously described (53). Sterile plants show a tight linkage to polymorphic markers IDP8472 and particularly IDP4279 that map to the end of the short arm of chromosome 5 on Bin 5.01 between physical positions 5.3 and 8.5 Mb. For each mutant, Mu insertions border sequences that cosegregate with the phenotype were determined using the Mu-Illumina border determination protocol as previously described (43).

RT-PCR analysis

RT-PCR analyses were conducted on RNA extracted using Trizol from meiotic anthers, as described (54). The *Afd1* 252bp cDNA, the *PhyC* 444bp cDNA fragments, and 3' and 5' portion of *Spo11-1* transcripts were amplified using specific primers (S1 Table). The *Phyc1* and *Phyc2* presented as two distinct bands from genomic DNA but with an identical size to cDNA. All PCRs were performed using DMSO and the Invitrogen GoTaq kit with 30 cycles using Tm= 52°C but for the SPO11-1 5' couple where Tm=60°C. Quantitative PCR of *Spo11-1 α* and *Spo11-1 β* transcripts was performed using FastStart Universal SYBR Green Master mix with specific primers (S1 Table). Cyanase was used as an internal normalization control. PCRs were performed on an ABI 7500 real-time PCR system in a 64-well reaction plate. The RT-qPCR reaction was performed in triplicate for each RNA sample. Specificity of the amplification products and Ct

values were analyzed using ABI prism dissociation curve analysis software.

Antibody production

To generate anti-SPO11-1 antibody, we used a peptide corresponding to amino acids 9-36 of SPO11-1 protein (RAAPLEGDEQQLRRRLEEAAALLLRRIKG) as antigen to generate a rabbit polyclonal antibody, followed by affinity purification (LTK BioLaboratories, Taiwan).

Western blot

Anthers were dissected from immature tassels after their meiotic stages and sizes were determined and snap frozen in liquid nitrogen. Protein extraction was performed as previously described (29). Two hundred micrograms of proteins were loaded in a 20 cm long, 10% SDS-PAGE gel, run for 18 h at 100 V, and then transferred to a polyvinylidene fluoride (PVDF) membrane. The PVDF membrane was blocked overnight with 5% milk in Tris-buffered saline-Tween (TBST) solution (containing 1X TBS and 0.1% Tween 20) at 4°C. Subsequently, the PVDF membrane was incubated with anti-SPO11-1 antibody (1:1000 dilution in 5% milk/TBST) and then with the horseradish peroxidase conjugated goat anti-rabbit IgG secondary antibody (1:5000 dilution in TBST). After a TBST wash, signals were detected using the UVP Biospectrum 600 imaging system.

Immunolocalization

Immature tassels were carefully removed from 4- to 6-week-old plants and kept in moist paper towel until dissection or fixation. Anthers were dissected after their meiotic stages and sizes were determined and their positions on a tassel were recorded as a relative time course. We analyzed meiosis in synchronized cohorts of meiocytes in anthers using characteristics described

previously (35) to precisely stage the progression of maize meiotic prophase in WT and mutant cells. Immunostaining was performed as described (55) with primary antibodies Anti-DSY2 (1:200), anti-ASY1 (1:400), Anti- γ H2AX (1:200), anti-RPA1 (1:200), anti-RAD51 (1:100), anti-AFD1 (1:200), anti-ZYP1 (1:100), and anti-SPO11-1 (1:100). The anti-RAD51 antibody was a gift from Wojciech Pawlowski (Cornell University) and anti- γ H2AX was a gift from Hong Ma and Yingxiang Wang (Fudan University). Conjugated secondary antibodies were obtained from Molecular Probes. Slides were imaged using either a LSM 780 with ELYRA equipped with SR-SIM (Zeiss) or a Deltavision core microscope (GE).

Image processing

The super-resolution z-stacking images were viewed with ZEN2012 software (Zeiss) to generate 2D projected images. To measure the distance between SPO11-1 and chromosome axes, the tool “ImageJ-FIJI” was used to generate SPO11-1 and DSY2 segmented 3D stack files. The 3D distance map was created using the plugin “3S Image Suite” (56), and distances between each SPO11-1 signal and nearby DSY2-labeled axes were analyzed using “3D manager” tool in 3D Image Suite.

TUNEL assay and TEM

The TUNEL assay for DSB detection was performed as described (57). First, meiocytes were embedded in polyacrylamide pads as described in the immunostaining protocol above. The TUNEL reaction was performed in a humid chamber for 2.5 h at 37°C with the *in Situ* Cell Death Detection Kit (Roche) using 100 μ L of reaction mixture per slide. Slides were mounted and imaged with a Deltavision core microscope. TEM analysis was performed as described (57, 58).

Authors Contributions:

AR wrote the paper, designed and carried out field, molecular experiments and immunocytological analyses. IG did the original forward genetic screen, determined the allelism between *mtm00-03* and *mtm99-14* and conducted initial cytological analyses of the *spo11-1* mutants. JCK generated and analyzed SPO11-1 antibody, performed immunolocalization and western blot, and carried out field works in Taiwan. DHL performed super-resolution microscopy and analyzed curly axial element in *spo11-1* mutant. LT made crosses, determined the allelism between *mtm00-03* and *mtm99-14*, conducted the TEM analysis and provided the DNA of the *mtm00-03* mutants for Mu-Illumina sequencing. AKGA did the RT-PCR analysis. YHK performed quantitative PCR for alternative splicing. KK did the BSA mapping and the RT-PCR analysis. RWC and AB did the Mu-Illumina border sequencing for *mtm99-14* and *mtm00-03*. RM provided the original seed stocks of the TUSC lines (*spo11-1-1*). ZC initiated the project. CJRW co-wrote the paper with AR and supervised the project.

Acknowledgments

We thank Jihyun Moon for advises on BSA mapping analysis. We thank Sidae Lee and Angel Jung for help with specimen collection for DNA sampling, and thank Patricia Elda Rueda for plant genotyping. We thank Wojtek Pawlowski, Hong Ma and Yingxiang Wang for their RAD51 and γ H2AX antibodies. We thank Shu-Chen Shen (Scientific Instrument Center, Academia Sinica) for help with super-resolution imaging. Special thanks to Thomas Boudier (Walter & Eliza Hall Institute, Australia) for his helps in image analysis using 3D Image Suite. We thank Mathilde Grelon for her valuable suggestions for this manuscript. This research was supported by a grant from NIH GM48547 (to WZC), a research grant from UNAM PAPIIT IA201217 (to AR), a grant IOS-1339130 from the US National Science Foundation (to AB), and

a grant (to CJRW) from Ministry of Science and Technology, Taiwan (107-2923-B-002-001-MY4).

Figures legends:

Figure 1. *mtm99-14* and *mtm00-03* are allelic and exhibit male and female infertility due to univalent formation during meiosis I.

(A) Male inflorescence (tassel) of the *mtm99-14* mutant and wild type at time of pollen shedding.

The wild type plants show protruding anthers and shed pollens. The mutant tassels rarely have protruding anthers that do not shed pollen grains.

(B) The first two ears on the left are from the heteroallelic *mtm99-14/mtm00-03* mutant pollinated with wild type pollens and mainly exhibit shriveled ovules. The last ear on the right is from a self-pollinated wild type plant.

(C) Acetocarmine staining of male meiocytes at metaphase I (upper panel) or tetrad stage (lower panel) of wild type, *mtm00-03*, *mtm99-14*, and heteroallelic *mtm99-14/mtm00-03* plants. In wild type male meiocytes, ten bivalents are aligned on a metaphase I plate and later produce normal tetrad cells. The mutants mainly present univalent chromosomes and rare interconnected chromosomes counted as bivalents (arrows). Univalents randomly segregate, leading to the formation of abnormal tetrads.

(D) Percentage of bivalents at metaphase I observed in mutants and wild type.

(E) Percentage of the different classes at tetrad stage in mutants and wild type.

Figure 2. Structure and expression of the SPO11-1 gene.

(A) Schematic drawing of the maize genomic region of chromosome 5. Both *mtm99-14* and

mtm00-03 mutants had Mu insertions, and remnants of Mu sequences (purple box) are associated with deletions (grey box) that entirely delete the *Phyc2* and *Spo11-1* genes. Coding regions and introns/UTRs are represented as orange and yellow boxes, respectively. The additional Mu insertion allele (*spo11-1-1*) is also indicated (red triangles). Green boxes represent transposable elements (Tourist and CACTA-like elements).

(B) RT-PCR analyses to amplify *Spo11-1* at 3' and 5' regions detected two spliced variants (asterisks). Afd1/Rec8 expression is used as a control.

(C) Quantitative PCR using specific primers showed differential expression of the *Spo11-1 α* and *Spo11-1 β* transcripts. Positions of primer sets are indicated in (D).

(D, E) Gene models (D) and predicted proteins (E) of SPO11-1 α and SPO11-1 β are shown. The additional region of SPO11-1 β (amino acid 73-115) is indicated as pink box.

(F) Western blot detected two SPO11-1 isoforms (arrowheads) in meiotic anthers. The entire blot is shown in Fig S5. The asterisk may be cross-reacted detection to SPO11-3 protein (436 amino-acid).

Figure 3. The *spo11-1* mutant is severely defective in DSB formation in maize.

(A-D) Meiocytes at zygotene stage of WT and the *spo11-1- Δ 03* mutant showing (A) TUNEL, (B) gamma-H2AX, (C) RPA1, and (D) RAD51 signals (all in green) and DAPI stained chromatin (red). The absence of signals in the *spo11-1* mutant suggested defective DSB formation. Scale bar represents 5 μ m.

Figure 4. The maize *spo11-1* mutant showed curly axial elements during early prophase I, whereas a similar structure appears transiently in wild-type leptotene.

(A, B) Immunostaining of DSY2 (green) in wild-type and *spo11-1- Δ 03* meiocytes. (A) The curly

morphology of axes is similar in WT and mutant when DSY2 first appears in nucleus at early leptotene. (B) At early zygotene, curly AEs are no longer observed in WT; however, the curly and spiral structures in mutant meiocytes are remained. Note that the intensity of DSY2 signals is aberrant, with some uneven and atypically bright fluorescent patches, which is distinct from the continuous smooth signals in WT (B).

(C) Similarly, ASY1 (green) staining also exhibited curly axial elements in the *spo11-1* mutant at early zygotene. To emphasize the curly morphology for mutant, a projection image containing ten Z-sections (1.5 μm) is shown.

Scale bar represents 5 μm .

Figure 5. Synapsis occurs promiscuously in *spo11-1* mutants.

(A-D) Immunostaining of ZYP1 (green) in wild-type (A, C) and *spo11-1- Δ 03* (B, D) meiocytes at early (A, B) and late pachytene (C, D). Note that ZYP1 loading starts mostly from one region of nucleus in wild-type, and extends through entire length of pachytene chromosomes. In contrast, ZYP1 signals in *spo11-1* mutants are short and discontinuous stretches. Scale bars represent 5 μm .

(E-G) Transmission electron microscopy of synaptonemal complex spreads of wild-type (E), *spo11-1- Δ 03* (F) and *spo11-1- Δ 14* (G). Higher magnifications from F and G are shown on the right. In contrast to complete synapsis in wild-type, both mutants revealed promiscuous synapsis (f' and g') and curly structure (f'' and g''). Note that synapsis can occur within one axis, forming “fold-back” structures (arrows in f' and g'), and promiscuous synapsis can be also seen as unequal synapsis with an overhang in mutants (arrowheads in f'). Scale bars represent 1 μm .

Figure 6. SPO11-1 localization and axial element structure are dynamic during leptotene.

(A-D) Immunostaining of SPO11-1 (green) in wild-type meiocytes at early leptotene (A), early zygotene (B), and pachytene (C) stages, as well as *spo11-1* mutant (D).

(E-F) Super resolution images of DSY2 (red) and SPO11-1 (green) in wild-type meiocytes at late leptotene (E), early zygotene (F). SPO11-1 signals first appear mostly around axial elements, which are shown in a magnified image (e). Note that the wild type axis morphology at this stage is still curly. At the leptotene-zygotene transition (F), telomere bouquet forms (single bracket in F). Note that most of the SPO11-1 foci are close to axial elements at this stage (f).

(G) Total numbers of SPO11-1 foci (blue box plots) remain similar in wild-type nuclei, but SPO11-1 loci associated with chromosome axes (red box plots) vary during early prophase I. A square represents the mean value.

Scale bars represent 5 μm (A-F), and 1 μm (e and f).

Supporting Data

Figure S1. Amplification of *PhyC* genes in wild-type (B73 and A344) and *spo11-1* mutants.

Both *PhyC1* and *PhyC2* genes were amplified using genomic DNA (gDNA) as template from B73 and A344 wild-types. 0P represents a negative control for PCR in absence of DNA template.

RT-PCR of *PhyC* gene expression and sequence analysis detected both *PhyC1* and *PhyC2* transcripts from cDNA of leaf (L) and anther (A) in wild-type (WT), in despite of one band. In contrast, sequencing results showed that only *PhyC1* transcript was detected in *mtm99-14* (14) and *mtm00-03* (03) mutants.

Figure S2. Acetocarmine staining of *spo11-1-1* allele during meiosis I.

(A) *spo11-1-1* meiocyte at pachytene.

(B-C) *spo11-1-1* meiocytes at diplotene.

(D-H) *spo11-1-1* meiocytes at diakinesis showed most univalents.

(I-L) *spo11-1-1* meiocytes at metaphase I showed most univalents.

Figure S3. Alignment of SPO11 amino acid sequences of maize (*Zm*), rice (*Os*), *Arabidopsis* (*At*), mouse (*Mm*) and human (*Hs*). The conserved residues are highlighted in red. The conserved tyrosine (Y) and WHD and TOPRIM domains are indicated. The 43 amino-acid additional domain in SPO11-1B is underlined (red).

Figure S4. Predicted structures of maize SPO11-1 β and SPO11-1 α isoforms. The predicted structures were obtained using Phyre2 and visualized using the PyMOL ‘cartoon’ (top) and ‘surface’ (bottom) tools. The SPO11-1 structure is based on the defined crystal structure of the TOPVIA protein of *Methanococcus jannaschii* (PDB model: c2zbkA). It forms a C shape that can dimerize to form a ring around DNA. The additional 43 amino-acids domain adds a protruding alpha-helix region opposite the groove containing the DNA binding region and the tyrosine catalytic site.

Figure S5. Western blot of SPO11-1 using protein extracts from meiotic anthers of the wild-type and *spo11-1- Δ 03* mutant.

Figure S6. Maize *spo11-1* allele showed almost absence of TUNEL or RAD51 signals.

(A) *spo11-1- Δ 03* male meiocyte showed complete absence of TUNEL signal.

(B) Around 10% of the *spo11-1* (here *spo11-1- Δ 03*) male meiocytes showed few TUNEL foci on chromatin (arrow).

(C-D) RAD51 immunolocalization for *spo11-1-Δ03* at zygotene. Around 10% of the mutant meiocytes show few RAD51 foci (D).

Scale bars represent 5 μm.

Figure S7. Immunostaining of AFD1, ASY1 and ZYP1 on *spo11-1* mutants showed curly axial elements and incomplete synapsis.

Figure S8. Super resolution microscopy showed that SPO11-1 localization and axial element structure are dynamic.

(A-B) Immunostaining of DSY2 (green) and SPO11-1 (red) in wild-type at mid-zygotene (A) and pachytene (B).

(C) Few SPO11-1 signals are detected in the *spo11-1Δ03* mutant. Note the curly axes in (D), magnified from (C). Scale bar represents 5 μm.

Movie S1. A series of z-stack deconvolution microscopy images of DSY2 signals at early leptotene of wild-type.

Movie S2. A series of z-stack deconvolution microscopy images of DSY2 signals at early leptotene of *spo11-1-Δ03* mutant.

Movie S3. A series of z-stack deconvolution microscopy images with SPO11 (green) and DAPI-stained chromatin (red) at early leptotene of wild-type.

Movie S4. A series of z-stack deconvolution microscopy images with SPO11 (green) and DAPI-stained chromatin (red) at leptotene-zygotene transition of wild-type.

Movie S5. A series of z-stack deconvolution microscopy images with SPO11 (green) and DAPI-stained chromatin (red) at pachytene of wild-type.

Movie S6. A series of z-stack deconvolution microscopy images with SPO11 (green) and DAPI-stained chromatin (red) at leptotene-zygotene transition of *spo11-1-Δ03* mutant.

Table. S1. Primers used in this study

<i>Afd1</i>	RW315	5'- TTATGCAGCTCTGGAAGGACT
	OH61	5'- GACTTCCAGGAGTAACACT ATGGTCACTGT
<i>PhyC</i>	AR105	5'- GTCATGCAAGGCATTCCTTTGGGCAAG
	AR106	5'- GCTGCTGAGCTGGGCGACCGGGAATC
<i>Spo11-1</i> (3')	AR101	5'- CAAACTTGTTGCGTGTCCC
	AR102	5'- AAGGAAATGGAATTTGCGG
<i>Spo11-1</i> (5')	AR103	5'- CTCCTCCGCAGGATCAAAGGGCTT
	AR104	5'- TGGCACGGTCAACAACACTGCTACTT
<i>Spo11-1α</i>	SPO11_ α F	5'- CCCATGTGCCTGCAGCT
	SPO11_ α R	5'- TGTGGAGCAGAGAGAGGACGT
<i>Spo11-1β</i>	SPO11_ β F	5'- CGCTCCCGGGATCATCT
	SPO11_ β R	5'- TGAAAATTGTTTCGAGGGATGTG
<i>Cyanase</i>	cyanaseF	5'- GCTGGTGAGGAGGAGAAACA
	cyanaseR	5'- CAGCAATCATGCCAGGTAGA

Table. S2 Average numbers of total SPO11-1 foci and SPO11-1 foci associated with axial elements.

	Mid-leptotene	Late leptotene	All leptotene	Mid-zygotene	Pachytene
<i>n</i>	6	8	14	7	6
SPO11-1 foci	290.2 \pm 81.6	356.4 \pm 73.7	328 \pm 81.5	302.1 \pm 86.5	312 \pm 84.6
SPO11-1 on AEs	209.7 \pm 69.4	266.4 \pm 85.21	240.1 \pm 81.3	205.3 \pm 46.6	66.7 \pm 40.7

References

1. Lam I, Keeney S. Mechanism and regulation of meiotic recombination initiation. *Cold Spring Harb Perspect Biol.* 2014;7(1):a016634.
2. Bergerat A, de Massy B, Gadelle D, Varoutas PC, Nicolas A, Forterre P. An atypical topoisomerase II from Archaea with implications for meiotic recombination. *Nature.* 1997;386(6623):414-417.
3. Gray S, Cohen PE. Control of Meiotic Crossovers: From Double-Strand Break Formation to Designation. *Annu Rev Genet.* 2016;50:175-210.
4. Lichten M, de Massy B. The Impressionistic Landscape of Meiotic Recombination. *Cell.* 2011;147(2):267-270.
5. Panizza S, Mendoza MA, Berlinger M, Huang L, Nicolas A, Shirahige K, et al. Spo11-Accessory Proteins Link Double-Strand Break Sites to the Chromosome Axis in Early Meiotic Recombination. *Cell.* 2011;146(3):372-383.
6. Smagulova F, Gregoret IV, Brick K, Khil P, Camerini-Otero RD, Petukhova GV. Genome-wide analysis reveals novel molecular features of mouse recombination hotspots. *Nature.* 2011;472(7343):375-378.
7. Pratto F, Brick K, Khil P, Smagulova F, Petukhova GV, Camerini-Otero RD. Recombination initiation maps of individual human genomes. *Science.* 2014;346(6211).
8. He Y, Wang M, Dukowic-Schulze S, Zhou A, Tiang CL, Shilo S, et al. Genomic features shaping the landscape of meiotic double-strand-break hotspots in maize. *Proc Natl Acad Sci U S A.* 2017;114(46):12231-12236.
9. Choi K, Zhao X, Tock AJ, Lambing C, Underwood CJ, Hardcastle TJ, et al. Nucleosomes and DNA methylation shape meiotic DSB frequency in *Arabidopsis thaliana* transposons and gene regulatory regions. *Genome Res.* 2018;28(4):532-546.
10. Pan J, Sasaki M, Kniewel R, Murakami H, Blitzblau HG, Tischfield SE, et al. A hierarchical combination of factors shapes the genome-wide topography of yeast meiotic recombination initiation. *Cell.* 2011;144(5):719-731.
11. Cooper TJ, Garcia V, Neale MJ. Meiotic DSB patterning: A multifaceted process. *Cell Cycle.* 2016;15(1):13-21.
12. Baudat F, Buard J, Grey C, Fledel-Alon A, Ober C, Przeworski M, et al. PRDM9 is a major determinant of meiotic recombination hotspots in humans and mice. *Science.* 2010;327(5967):836-840.

13. Li J, Hooker GW, Roeder GS. *Saccharomyces cerevisiae* Mer2, Mei4 and Rec114 form a complex required for meiotic double-strand break formation. *Genetics*. 2006;173(4):1969-1981.
14. Kee K, Protacio RU, Arora C, Keeney S. Spatial organization and dynamics of the association of Rec102 and Rec104 with meiotic chromosomes. *EMBO J*. 2004;23(8):1815-1824.
15. Kim KP, Weiner BM, Zhang L, Jordan A, Dekker J, Kleckner N. Sister Cohesion and Structural Axis Components Mediate Homolog Bias of Meiotic Recombination. *Cell*. 2010;143(6):924-937.
16. Miyoshi T, Ito M, Kugou K, Yamada S, Furuichi M, Oda A, et al. A central coupler for recombination initiation linking chromosome architecture to S phase checkpoint. *Mol Cell*. 2012;47(5):722-733.
17. Keeney S, Lange J, Mohibullah N. Self-Organization of Meiotic Recombination Initiation: General Principles and Molecular Pathways. *Annual Review of Genetics*. 2014;48(1):187-214.
18. Brar GA, Kiburz BM, Zhang Y, Kim J-E, White F, Amon A. Rec8 phosphorylation and recombination promote the step-wise loss of cohesins in meiosis. *Nature*. 2006;441(7092):532-536.
19. Chelysheva L, Diallo S, Vezon D, Gendrot G, Vrielynck N, Belcram K, et al. AtREC8 and AtSCC3 are essential to the monopolar orientation of the kinetochores during meiosis. *J Cell Sci*. 2005;118(20):4621-4632.
20. Golubovskaya IN, Hamant O, Timofejeva L, Wang C-JR, Braun D, Meeley R, et al. Alleles of *afd1* dissect REC8 functions during meiotic prophase I. *J Cell Sci*. 2006;119(16):3306-3315.
21. Armstrong SJ, Caryl AP, Jones GH, Franklin FC. *Asy1*, a protein required for meiotic chromosome synapsis, localizes to axis-associated chromatin in *Arabidopsis* and *Brassica*. *J Cell Sci*. 2002;115(Pt 18):3645-3655.
22. Nonomura K, Nakano M, Eiguchi M, Suzuki T, Kurata N. PAIR2 is essential for homologous chromosome synapsis in rice meiosis I. *J Cell Sci*. 2006;119(Pt 2):217-225.
23. Shin YH, Choi Y, Erdin SU, Yatsenko SA, Kloc M, Yang F, et al. *Hormad1* mutation disrupts synaptonemal complex formation, recombination, and chromosome segregation in mammalian meiosis. *PLoS Genet*. 2010;6(11):e1001190.
24. Wojtasz L, Daniel K, Roig I, Bolcun-Filas E, Xu H, Boonsanay V, et al. Mouse HORMAD1 and HORMAD2, two conserved meiotic chromosomal proteins, are depleted from synapsed chromosome axes with the help of TRIP13 AAA-ATPase. *PLoS Genet*. 2009;5(10):e1000702.

25. Golubovskaya IN, Wang CJ, Timofejeva L, Cande WZ. Maize meiotic mutants with improper or non-homologous synapsis due to problems in pairing or synaptonemal complex formation. *J Exp Bot.* 2011;62(5):1533-1544.
26. Yang F, Fuente RDL, Leu NA, Baumann C, McLaughlin KJ, Wang PJ. Mouse SYCP2 is required for synaptonemal complex assembly and chromosomal synapsis during male meiosis. *J Cell Biol.* 2006;173(4):497-507.
27. Kouznetsova A, Novak I, Jessberger R, Hoog C. SYCP2 and SYCP3 are required for cohesin core integrity at diplotene but not for centromere cohesion at the first meiotic division. *J Cell Sci.* 2005;118(Pt 10):2271-2278.
28. Wang K, Wang M, Tang D, Shen Y, Qin B, Li M, et al. PAIR3, an axis-associated protein, is essential for the recruitment of recombination elements onto meiotic chromosomes in rice. *Mol Biol Cell.* 2011;22(1):12-19.
29. Lee DH, Kao YH, Ku JC, Lin CY, Meeley R, Jan YS, et al. The Axial Element Protein DESYNAPTIC2 Mediates Meiotic Double-Strand Break Formation and Synaptonemal Complex Assembly in Maize. *Plant Cell.* 2015;27(9):2516-2529.
30. Ferdous M, Higgins JD, Osman K, Lambing C, Roitinger E, Mechtler K, et al. Inter-homolog crossing-over and synapsis in Arabidopsis meiosis are dependent on the chromosome axis protein AtASY3. *PLoS Genet.* 2012;8(2):e1002507.
31. Lambing C, Osman K, Nuntasontorn K, West A, Higgins JD, Copenhaver GP, et al. Arabidopsis PCH2 Mediates Meiotic Chromosome Remodeling and Maturation of Crossovers. *PLoS Genet.* 2015;11(7):e1005372.
32. Miao C, Tang D, Zhang H, Wang M, Li Y, Tang S, et al. Central region component1, a novel synaptonemal complex component, is essential for meiotic recombination initiation in rice. *Plant Cell.* 2013;25(8):2998-3009.
33. Ji J, Tang D, Shen Y, Xue Z, Wang H, Shi W, et al. P31comet, a member of the synaptonemal complex, participates in meiotic DSB formation in rice. *Proc Natl Acad Sci U S A.* 2016;113(38):10577-10582.
34. de Massy B. Initiation of meiotic recombination: how and where? Conservation and specificities among eukaryotes. *Annu Rev Genet.* 2013;47:563-599.
35. Dawe RK, Sedat JW, Agard DA, Cande WZ. Meiotic chromosome pairing in maize is associated with a novel chromatin organization. *Cell.* 1994;76(5):901-912.
36. Wang CJ, Carlton PM, Golubovskaya IN, Cande WZ. Interlock formation and coiling of meiotic chromosome axes during synapsis. *Genetics.* 2009;183(3):905-915.
37. Phillips D, Nibau C, Wnetrzak J, Jenkins G. High resolution analysis of meiotic chromosome structure and behaviour in barley (*Hordeum vulgare* L.). *PLoS One.* 2012;7(6):e39539.

38. Higgins JD, Osman K, Jones GH, Franklin FC. Factors underlying restricted crossover localization in barley meiosis. *Annu Rev Genet.* 2014;48:29-47.
39. Colas I, Shaw P, Prieto P, Wanous M, Spielmeier W, Mago R, et al. Effective chromosome pairing requires chromatin remodeling at the onset of meiosis. *Proc Natl Acad Sci U S A.* 2008;105(16):6075-6080.
40. Ronceret A, Pawlowski WP. Chromosome dynamics in meiotic prophase I in plants. *Cytogenet Genome Res.* 2010;129(1-3):173-183.
41. Golubovskaya IN, Sheridan WF, Harper LC, Zacheus CW. Novel meiotic mutants of maize identified from Mu transposon and EMS mutant screens. *Maize Genet Coop Newsl* 2003 77:10–13.
42. Cande WZ, Golubovskaya I, Wang CJR, Harper L. Meiotic Genes and Meiosis in Maize. In: Bennetzen J, Hake S, editors. *Handbook of Maize.* New York: Springer; 2009. p. 353-375.
43. Williams-Carrier R, Stiffler N, Belcher S, Kroeger T, Stern DB, Monde RA, et al. Use of Illumina sequencing to identify transposon insertions underlying mutant phenotypes in high-copy Mutator lines of maize. *Plant J.* 2010;63(1):167-177.
44. McCarty DR, Meeley RB. Transposon Resources for Forward and Reverse Genetics in Maize. In: Bennetzen JL, Hake S, editors. *Handbook of Maize: Springer New York;* 2009. p. 561-584.
45. Hiraoka T. Studies of mitosis and meiosis in comparison. III. Behaviour of chromonemata in the pre-leptotene state in meiosis. *Cytologia (Tokyo)* 1941;11:473-482.
46. Walters MS. Evidence on the time of chromosome pairing from the preleptotene spiral stage in *Lilium longiflorum* "Croft". *Chromosoma.* 1970;29(4):375-418.
47. Simanovsky SA, Matveevsky SN, Iordanskaya IV, Spangenberg VE, Kolomiets OL, Bogdanov YF. Spiral cores of synaptonemal complex lateral elements at the diplotene stage in rye include the ASY1 protein. *Russ J Genet.* 2014;50(10):1107-1111.
48. Church K. Meiosis in the grasshopper. II. The preleptotene spiral stage during oogenesis and spermatogenesis in *Melanoplus femur-rubrum*. *Can J Genet Cytol.* 1972;14(2):397-401.
49. Franklin AE, McElver J, Sunjevaric I, Rothstein R, Bowen B, Cande WZ. Three-dimensional microscopy of the Rad51 recombination protein during meiotic prophase. *Plant Cell.* 1999;11(5):809-824.
50. Pawlowski WP, Golubovskaya IN, Cande WZ. Altered nuclear distribution of recombination protein RAD51 in maize mutants suggests the involvement of RAD51 in meiotic homology recognition. *Plant Cell.* 2003;15(8):1807-1816.
51. Chen C, Jomaa A, Ortega J, Alani EE. Pch2 is a hexameric ring ATPase that remodels the chromosome axis protein Hop1. *Proc Natl Acad Sci U S A.* 2014;111(1):E44-53.

52. Joshi N, Brown MS, Bishop DK, Borner GV. Gradual implementation of the meiotic recombination program via checkpoint pathways controlled by global DSB levels. *Mol Cell*. 2015;57(5):797-811.
53. Moon J, Skibbe D, Timofejeva L, Wang CJ, Kelliher T, Kremling K, et al. Regulation of cell divisions and differentiation by MALE STERILITY32 is required for anther development in maize. *Plant J*. 2013;76(4):592-602.
54. Nan GL, Ronceret A, Wang RC, Fernandes JF, Cande WZ, Walbot V. Global transcriptome analysis of two ameiotic1 alleles in maize anthers: defining steps in meiotic entry and progression through prophase I. *BMC Plant Biol*. 2011;11:120.
55. Wang CJ. Analyzing maize meiotic chromosomes with super-resolution structured illumination microscopy. *Methods Mol Biol*. 2013;990:67-78.
56. Ollion J, Cochenec J, Loll F, Escude C, Boudier T. TANGO: a generic tool for high-throughput 3D image analysis for studying nuclear organization. *Bioinformatics*. 2013;29(14):1840-1841.
57. Pawlowski WP, Golubovskaya IN, Timofejeva L, Meeley RB, Sheridan WF, Cande WZ. Coordination of meiotic recombination, pairing, and synapsis by PHS1. *Science*. 2004;303(5654):89-92.
58. Timofejeva L, Grebennikova ZK, Gaft M, Golubovskaya I. Ultrastructural features of synaptonemal complexes of maize in norm. *Tsitol Genet/Cytol Genet*. 1991;33(6):12-19.

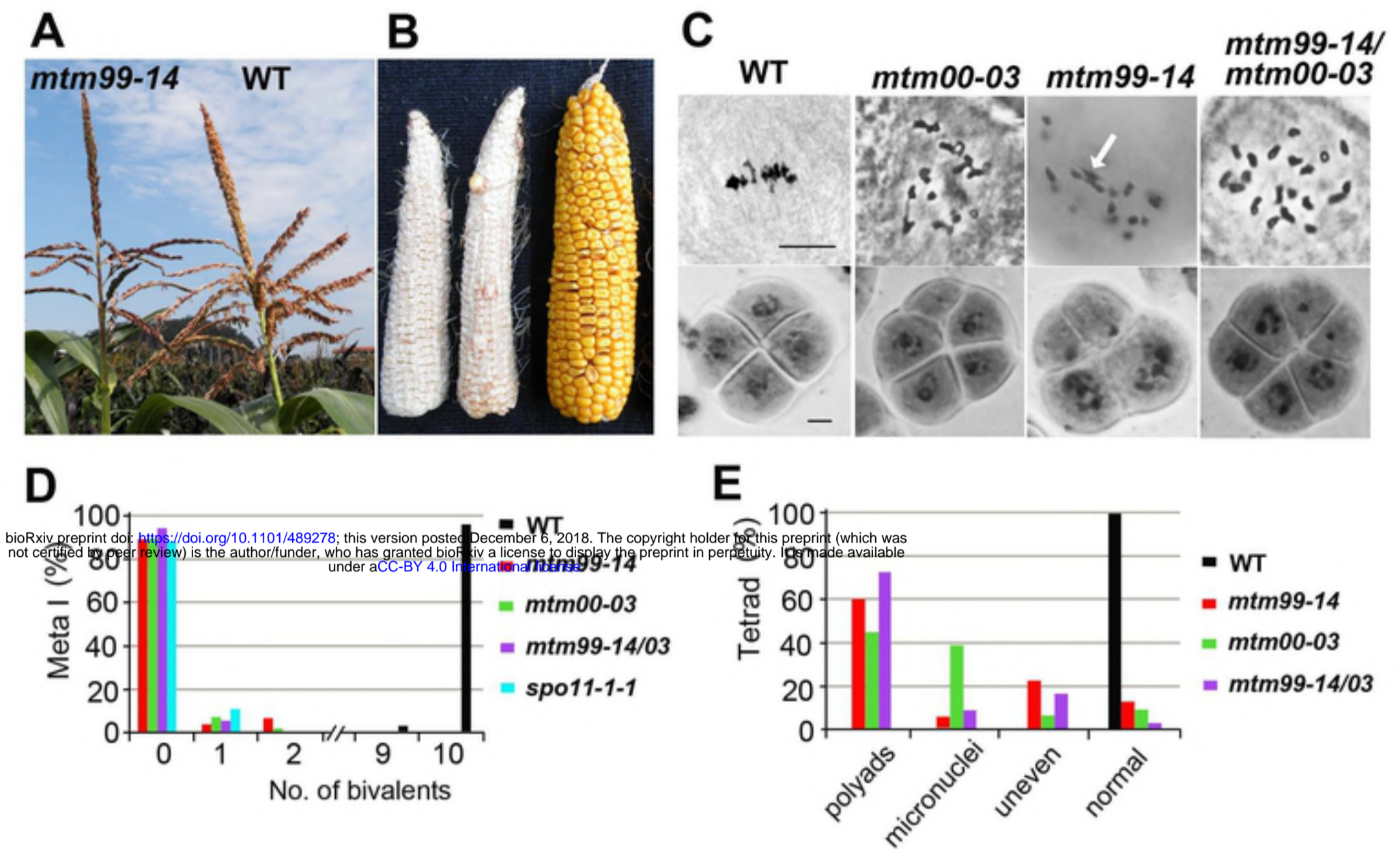


Figure 1. *mtm99-14* and *mtm00-03* are allelic and show male and female infertility due to univalent formation during meiosis I.

(A) Male inflorescence (tassel) of the *mtm99-14* mutant and wild type at time of pollen shedding. The wild type plant show protruding anthers and shed pollens. The mutant tassels have very rare protruding anthers that do not shed pollen grains.

(B) The first two ears on the left are from the heteroallelic *mtm99-14/mtm00-03* mutant pollinated with wild type pollens and mainly exhibit shriveled ovules. The last ear on the right is from a self-pollinated wild type plant.

(C) Acetocarmine staining of male meiocytes at metaphase I (upper panel) or tetrad stage (lower panel) of wild type, *mtm00-03*, *mtm99-14*, and heteroallelic *mtm99-14/mtm00-03* plants. In wild type male meiocytes, ten bivalents are aligned on metaphase I plate and later produce normal tetrad cells. The mutants show mainly univalents chromosomes and rare interconnected chromosomes counted as bivalents (arrows). Univalents randomly segregate, leading to the formation of abnormal tetrads.

(D) Percentage of bivalents at metaphase I observed in mutants and wild type.

(E) Percentage of the different classes at tetrad stage in mutants and wild type.